View metadata, citation and similar papers at core.ac.uk

brought to you by CORE

東北大学機関リポジトリ TOUR Tohoku University Repository

Imaging of optical and topographical distributions by simultaneous near field scanning optical/atomic force microscopy with a microfabricated photocantilever

著者	桑野　博喜
journal or publication title	Journal of applied physics
volume	78
number	12
page range	7376-7381
year	1995
URL	http://hdl.handle.net/10097/35253

doi: 10.1063/1.360387

Imaging of optical and topographical distributions by simultaneous near field scanning optical/atomic force microscopy with a microfabricated photocantilever

Kenji Fukuzawa,[a] Yuriko Tanaka, Shinya Akamine,[b] and Hiroki Kuwano
Nippon Telegraph and Telephone Corporation, Interdisciplinary Research Laboratories, 3-9-11 Midori-cho, Musashino-shi, Tokyo 180, Japan

Hirofumi Yamada
National Institute for Advanced Interdisciplinary Research, 1-1-4 Higashi, Tsukuba 305, Japan

(Received 16 March 1995; accepted for publication 11 September 1995)

Simultaneous near field scanning optical and atomic force microscopy with a microfabricated photocantilever reveal both optical and topographical distributions. The cantilever tip changes the evanescent field into scattering light, and this scattering light is detected with a photodiode fabricated in the tip of the cantilever. The cantilever deflection signal leads to atomic force images. The resolution for imaging the evanescent field variation was 20 nm ($\lambda/30$). The near field optical and atomic force images indicate that the same point of the cantilever tip generates both optical and atomic force signals. This method is a new approach to optical and topographical microscopy with nanometer resolution. © *1995 American Institute of Physics.*

I. INTRODUCTION

Near field scanning optical microscopy (NSOM), which is a type of scanning probe microscopy, has been anticipated to provide optical characteristic distributions of samples with nanometer resolution. Atomic force microscopy (AFM) also produces sample images with angstrom resolution, which provides topographic information about samples.[1] Obtaining both optical and topographical distributions is very useful in characterizing samples. Various methods for distance regulation in NSOM have been presented. Recently, sharpened micropipettes or optical fibers have been used for NSOM/AFM observation. Methods using a bent micropipette with an optical level method[2] and a micropipette or an optical fiber with shearing force regulation have been reported.[3–5] Bending a fiber causes loss of collected or illumination light power for NSOM. The latter method requires vibration of the tip. Another approach is to control the distance by the tunneling current to NSOM.[6,7] However, this method is not applicable to nonconductive samples, and many optical materials are nonconductive.

Recently, a semiconductor probe detector for NSOM had been presented.[8] They fabricated a submicrometer Al–Si Schottkey diode to make the photodetector size smaller. We recently proposed a new type of NSOM probe, a microfabricated photocantilever,[9] which is a cantilever with a photodiode. When the tip of the photocantilever approaches to the evanescent field, the photodiode in the cantilever detects the scattering light from the tip of the cantilever. The high resolution capability of a light-scattering type NSOM had recently been demonstrated.[10–12] We placed the scattering center very close to the detector using micromachining techniques. This enables us to make the collection angle of the detector several times larger, compared with the collection angle of the setup reported by van Hulst *et al.*[10] [a 0.5 numerical aperture (N.A.) microscope objective] so our photocantilever had been able to collect much more scattering light. In addition, a well-established optical lever method is easily applied to the photocantilever for atomic force detection because it is very similar to a widely used AFM cantilever. The photodiode in the tip of the cantilever detects the evanescent field distribution modulated by the sample. The cantilever deflection signal produces atomic force images. The photocantilever is very suitable for NSOM/AFM imaging and also for mass production. This paper demonstrates the simultaneous optical and topographical imaging capabilities of the photocantilever.

II. RESULTS AND DISCUSSION

A. Experimental setup

Our experimental setup is shown in Fig. 1. The inset in Fig. 1 shows a perspective view of the photocantilever. A 2 mW He–Ne laser (wavelength: 633 nm) was used as a light source. It was arranged so that the incident light would undergo total internal reflection (TIR) on the dove prism surface, generating the evanescent field onto the prism surface. The taper angle of the dove prism (γ in Fig. 1) was selected to be 40°, and the incident angle of the laser beam was 70.7°. The evanescent field transmitted through the sample was detected by the photodiode at the tip of the photocantilever. The fabricated photodiode was a Si-based pn-junction type. Details of the cantilever structure have been published elsewhere.[9] The tip of the cantilever disturbed the evanescent field transmitted through the sample, changing it into scattered light. This scattered light is absorbed by the photodiode. The cantilever deflection is detected by a standard optical lever method using a combination of a laser diode and a two-segment photodiode. Our cantilever was 1500 μm long, 100 μm wide, and 5 μm thick. Its calculated spring constant was 0.2 N/m. It was a flat cantilever with no microprotrusions, so the tip of the cantilever was used as the scattering

[a]Author to whom correspondence should be addressed.
[b]Present address: P.O. Box 7704, Stanford, CA 94309.

 © 1995 American Institute of Physics

Downloaded 15 Oct 2008 to 130.34.135.158. Redistribution subject to AIP license or copyright; see http://jap.aip.org/jap/copyright.jsp

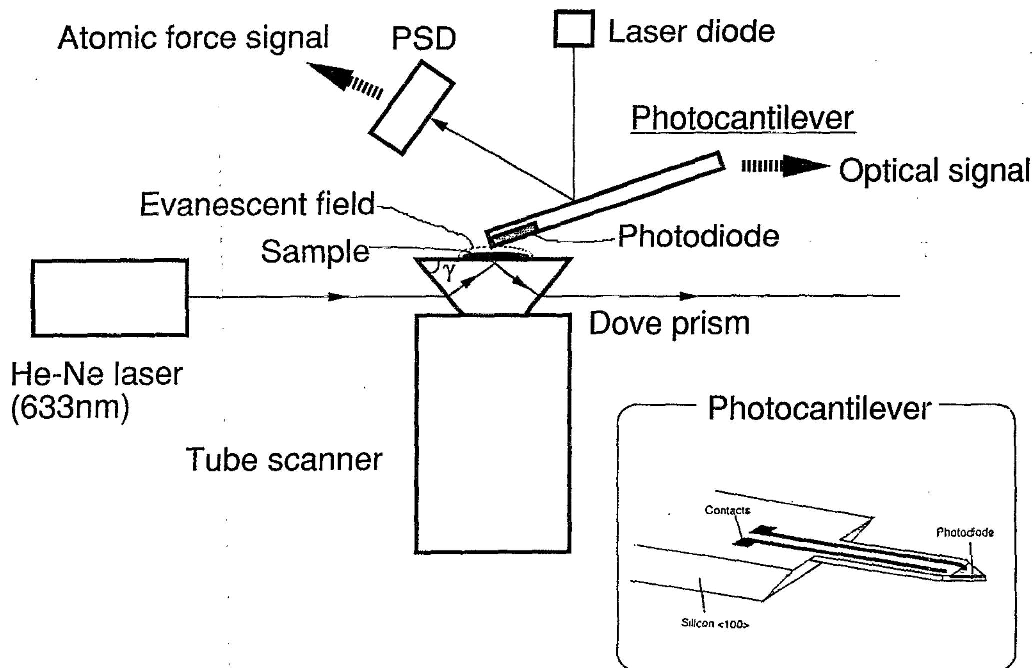

FIG. 1. Setup for simultaneous NSOM/AFM. Taper angle γ of dove prism was 40°. Inset shows perspective view of photocantilever.

center. Samples were scanned with a tube scanner. In this setup, the laser spot for the optical lever was shifted so far from the tip of the photocantilever that the intensity of the laser for the optical lever could be neglected compared with the detected evanescent light intensity. The typical shift was about 750 μm, which was about half the length of the cantilever. This enabled us to obtain NSOM and AFM signals, simultaneously. Sample images were obtained in the contact AFM mode, and the constant force regulation was used. The gap between the sample and the prism surface was filled with index matching oil.

B. Expression of NSOM/AFM images

In order to interpret an NSOM image, it is useful to consider its expected expression. The intensity of the NSOM signal is:

$$I(x,y,z) \approx \eta I_0 T[x,y,h(x,y)] D[z-h(x,y)], \tag{1}$$

where η is the detection efficiency of the photocantilever, I_0 is incident evanescent light intensity, $T(x,y,h)$ is the transmittance distribution of the sample, $h(x,y)$ is the sample thickness, and $D(z)$ is the decay function of the evanescent field above the sample. The normal direction of a prism plane is defined here as the z-axis and z is the distance between the cantilever tip and the prism surface. The $h(x,y)$ is a function of the tip position (x,y) on the sample and represents a topographic image of the sample. When we use the contact AFM mode, z is always equal to $h(x,y)$, so $D(z)$ is equal to $D(0)$. Equation (1) shows that an image obtained by NSOM is not always a pure optical characteristic distribution but a distribution mixed with a topographic one if the tip makes contact with the sample surface during imaging. Therefore, interpretation of an NSOM image requires knowledge of the topographic distribution.

C. Optical- and force-distance curves

Figures 2(a) and 2(b) show the relationship between the z-dependence of the optical intensity and the atomic force. Multiplying the deflection with the spring constant, the atomic force was determined. The horizontal axes show z-scan control signals. There was no sample on the prism in this case. The photocantilever approached the prism surface from the left side in the figure. The slope of the force–distance curve changed after the tip of the photocantilever made contact with the prism surface, and simultaneously, the optical signal was saturated. Hysteresis caused by the adhesion force in the water film layer on the prism surface was observed in both optical and force signals. In the force signal, cantilever oscillation was observed after the tip was removed. In the optical signal, the intensity was too low to detect the cantilever oscillation. The removal point from the water film layer in Fig. 2(a) was identical to that in Fig. 2(b). This good correlation indicates that the same point in the photocantilever contributes to both NSOM and AFM signals. Since there was no sample in this case, $T(x_0,y_0)$ is unity. In this case, Eq. (1) could be approximated to the following equation:

$$I(x_0,y_0,h) \approx \eta I_0 \exp(-\mu_0 z), \tag{2}$$

where μ_0^{-1} was about 40 nm for our setup. This exponential decay of the optical intensity shows that the photocantilever detects the evanescent field on the prism.

Downloaded 15 Oct 2008 to 130.34.135.158. Redistribution subject to AIP license or copyright; see http://jap.aip.org/jap/copyright.jsp

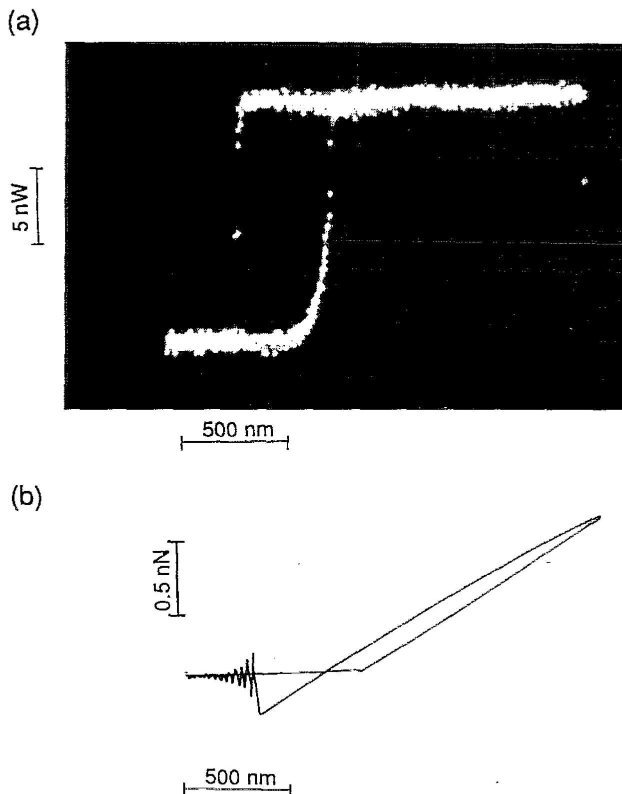

FIG. 2. Optical– and force–distance curves. (a) Optical–distance curve. (b) Force–distance curve. Hysteresis caused by adhesion force of water film layer on prism was observed in both curves.

D. Simultaneous NSOM/AFM imaging

NSOM/AFM images of a variety of samples were obtained. Figure 3 shows the high resolution capability of our NSOM with the photocantilever. The images are NSOM/AFM images of small dust particles on a prism. Bright points in the NSOM image are points of high optical intensity, and bright points in the AFM image are swelling points—the correlation is very good. Corresponding points in the figures are located at the same position. This agrees with the results obtained in Fig. 2. Figures 3(c) and 3(d) show the cross-sectional view of Figs. 3(a) and 3(b). They are the images on the diagonal line from the left upper edge to the right lower edge. In Figs. 3(c) and 3(d), gaps of about 20 nm can be resolved (marked by arrows). This is about 1/30 of the wavelength. This data was obtained on a sample with topography, so the obtained NSOM image was affected by both the refractive index and topographic variations of the sample. Therefore, this data does not directly indicate that the resolution of our NSOM for imaging the refractive index distribution is better than 20 nm. However, it at least indicates that the resolution of our NSOM for imaging the evanescent field distribution is better than 20 nm, since our NSOM is sensitive to the evanescent field distribution. In Fig. 3(e), the relationship between the NSOM signal and the tip height from the prism is shown. Comparing the NSOM and AFM images, we obtained the height and NSOM signal of the target point. This is roughly approximated by $\exp(-\mu_1 h)$, where μ_1^{-1} is 5 nm. The value of μ_1 is much larger than μ_0 mentioned in Eq. (2). If we assume that dust particles only absorb the evanescent light, then $T(x,y,h)=\exp(-\alpha h)$, where the absorbance coefficient of particles is α. In this case, Eq. (1) is given as

$$I(x,y,h)\approx \eta I_0 \exp(-\alpha h). \tag{3}$$

According to this assumption, the absorbance coefficient of particles α is about 0.2 nm^{-1}. The absorbance of metal is of the same order as this value, so this assumption is reasonable if the particles were made of metals.

Figures 4(a) and 4(b) show the capability of our NSOM to image the refractive index distribution. They show NSOM/AFM images of recorded pits on a phase-change (PC) optical disk. The recording layer consists of $GeTe\text{-}Sb_2Te_3\text{-}Sb$.[13] We recorded pits in a gratingless area of the inner part of the disk. After recording, resin and aluminum-reflection layers were removed from the disk. Applying Eq. (1) to this case, we found that $T(x,y,h)$ varies with position (x,y), whereas $h(x,y)$ is constant because the disk surface was expected to be topographically flat. The pit region is in the amorphous phase; whereas, the other region is in the crystal phase. The refractive indices of the pit region and the other region are $4.9+1.4i$ and $5.7+3.4i$, respectively. In Fig. 4, index changes in the pit region are visible by NSOM, and AFM showed that the disk surface is topographically flat. The resolution of NSOM was lower in Fig. 4 than in Fig. 3, due to the interference between pits and the multiple interferences caused by the multilayer structure of the disk. The disk consists of the recording layer, the dielectric layer, and the substrate. Other samples should be used to evaluate the resolution of the NSOM for imaging the refractive index distribution.

Figures 5(a) and 5(b) show NSOM/AFM images of a grating of the PC optical disk mentioned above. The grating pitch is 1600 nm and the groove width is 800 nm. AFM reveals that the land is about 85 nm higher than the groove. In contrast, NSOM shows that the evanescent light intensity of the land is much lower than that of the groove. One simple explanation for the interpretation of the NSOM image is that the incident light decays in the land. In the groove, the incident light undergoes TIR under the groove surface; whereas, it will propagate toward the land surface in the land. Assuming that a land plays the role of a slit for the incident light, the incident wave cannot propagate through the land when the land width, i.e., the "slit" is similar or smaller than the wavelength of the light. In our experiment, the land width (800 nm) was similar to the wavelength (633 nm). In contrast, the incident light in the groove part was detected by the photocantilever, since it does not experience the decay due to the slit effect. By using Fourier optics theory,[14] the decay length in the land is given by

$$\mu_2^{-1}=\frac{\dfrac{\lambda}{n\cos\theta}}{4\pi\sqrt{\left(\dfrac{\lambda}{an\cos\theta}\right)^2-1}}, \tag{4}$$

where a is the land width, θ is the incident angle of the

Downloaded 15 Oct 2008 to 130.34.135.158. Redistribution subject to AIP license or copyright; see http://jap.aip.org/jap/copyright.jsp

(a) (b)

200 nm 200 nm

(c)

5 nW

200 nm

(d)

10 nm

200 nm

(e)

Near-field Signal (nW)

Sample Height (nm)

FIG. 3. NSOM/AFM images of small particles on prism. (a) NSOM image. (b) AFM image. (c) and (d) are cross-sectional views of (a) and (b) [On diagonal line from upper left edge to lower right edge in (a) and (b)]. Approximate 20 nm gaps between particles could be resolved (arrow). (e) Relationship between NSOM signal and cantilever height from prism surface.

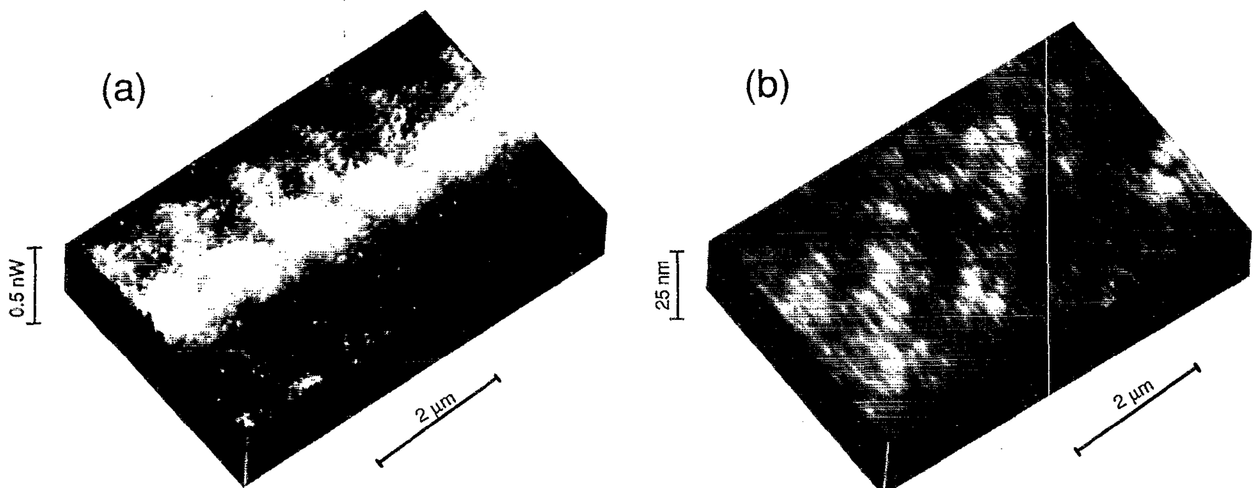

FIG. 4. NSOM/AFM images of pits on a phase-change optical disk. (a) NSOM image. (b) AFM image. Pit image was observed by NSOM but AFM showed that disk surface was topographically flat.

Downloaded 15 Oct 2008 to 130.34.135.158. Redistribution subject to AIP license or copyright; see http://jap.aip.org/jap/copyright.jsp

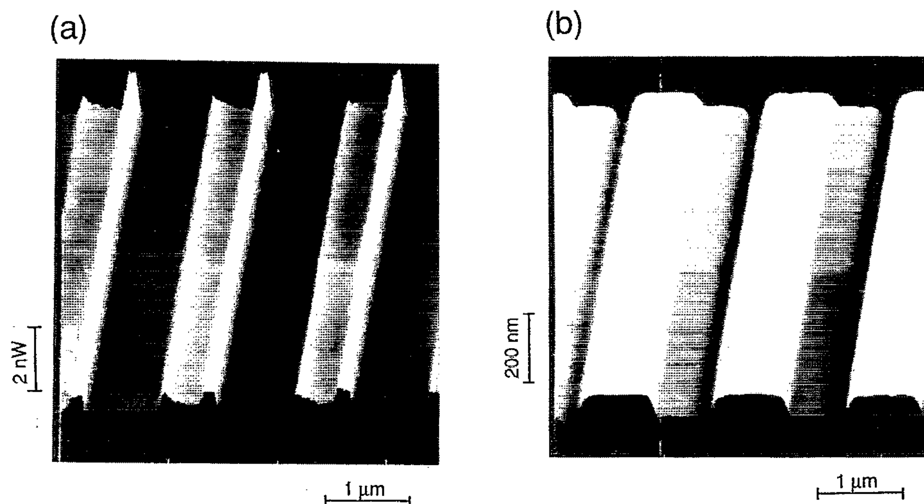

FIG. 5. NSOM/AFM images of gratings of a phase-change optical disk. (a) NSOM image. (b) AFM image. (c) Relationship between NSOM signal and cantilever height from the groove surface.

light, n is the refractive index of the disk substrate, and λ is the wavelength. Therefore, the expected NSOM intensities in the land and groove I_l and I_g are given by

$$I_l(x,y,h_l) \approx \eta I_0 T_0 \exp(-\mu_2 h_l), \tag{5}$$

$$I_g(x,y,0) \approx \eta I_0 T_0, \tag{6}$$

where h_l is the difference in height between the land and groove. Here, the z-origin is defined as the groove surface. Applying Eq. (4) to our setup, the calculated μ_2^{-1} is about 84 nm for $n=1.5$, $\theta=70.7°$, $a=800$ nm, and λ-633 nm. This calculated decay length is the same order as the land height. This indicates that our simple model can provide a reasonable explanation of the difference between the NSOM/AFM images.

Figures 6(a) and 6(b) show an example using NSOM/AFM for biological materials. Imaging the fine structure of biological materials is one of the most important targets for NSOM/AFM. The images are monolayers of purple membranes,[15,16] that is a cell membrane obtained from the bacterium *Halobacterium salinarium*. A purple membrane is a two-dimensional crystal that consists of proteins and a lipid bilayer. The monolayer membranes were obtained by dropping a purple membrane solution of appropriate density onto the prism and drying its surface in air. The AFM image indicates that the thickness of the monolayer is about 5 nm, which agrees well with previously reported values. Both NSOM and AFM clearly reveal that this purple membrane has small defect holes whose diameters are on the order of 10 nm. This supports the fact that the resolution of our NSOM for imaging the evanescent field variation is better than 20 nm, as mentioned in Fig. 3.

III. SUMMARY

We have demonstrated simultaneous NSOM/AFM imaging with a photocantilever (a microfabricated cantilever with a pn-junction at its tip). The resolution for imaging the eva-

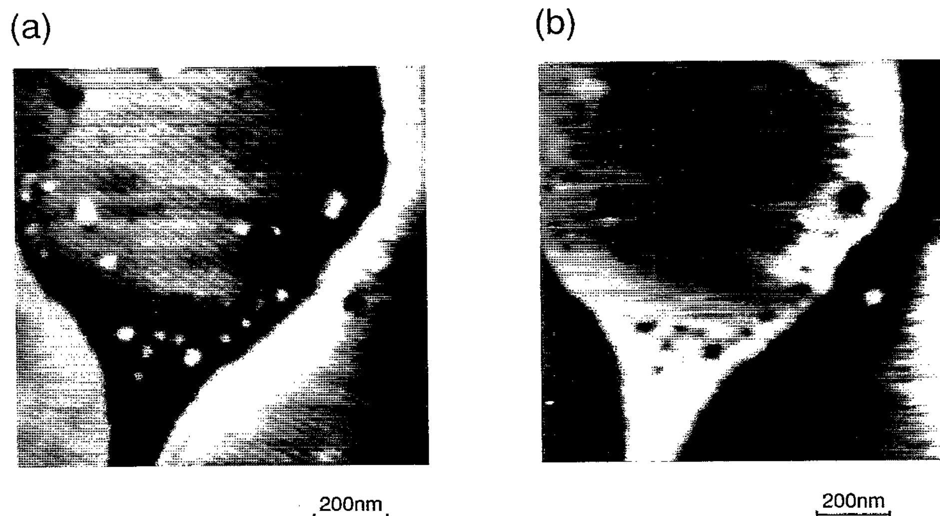

FIG. 6. NSOM/AFM images of monolayer purple membranes. (a) NSOM image. (b) AFM image. Thickness of a purple membrane is about 5 nm.

Downloaded 15 Oct 2008 to 130.34.135.158. Redistribution subject to AIP license or copyright; see http://jap.aip.org/jap/copyright.jsp

nescent field variation was 20 nm (λ/30). The optical and topographic images indicate that the same point at the tip of the cantilever generates both optical and atomic force signals. Our NSOM could image the refractive index distribution. This method is a new approach to optical and topographical microscopy with nanometer resolution.

ACKNOWLEDGMENTS

We would like to thank N. Kakuta and T. Yoshimura for their aid with the photocantilever fabrication. We also thank K. Tanabe for sample preparation of the PC-optical disk preparation.

[1] For instance, *Scanning Tunneling Microscopy II*, edited by R. Wiesendanger and H.-J. Guntherodt (Springer, Berlin, 1992).
[2] S. Shalom, K. Liberman, and A. Lewis, Rev. Sci. Instrum. **63**, 4061 (1992).
[3] P. C. Yang, Y. Chen, and M. Vaez-Iravani, J. Appl. Phys. **71**, 2499 (1992).
[4] E. Betzig, P. Finn, and J. S. Weiner, Appl. Phys. Lett. **60**, 2484 (1992).
[5] R. Told-Crow, P. C. Yang, Y. Chen, and M. Vaez-Iravani, Appl. Phys. Lett. **60**, 2957 (1992).
[6] U. Durig, D. W. Pohl, and F. Rohner, J. Appl. Phys. **59**, 3318 (1986).
[7] K. Liberman and A. Leiws, Appl. Phys. Lett. **62**, 1335 (1993).
[8] R. C. Davis, C. C. Williams, and Neuzil, Appl. Phys. Lett. **66**, 2309 (1995).
[9] S. Akamine, H. Kuwano, K. Fukuzawa, and H. Yamada, Proc. IEEE Micro Electro Mechan. Systems, 1995, p. 145; S. Akamine, H. Yamada, and H. Kuwano, Appl. Phys. Lett. (to be published).
[10] N. F. van Hulst, M. H. Moers, O. F. Noordham, R. G. Tack, F. B. Segerink, and B. Bolger, Appl. Phys. Lett. **62**, 461 (1993).
[11] F. Zenhausern, M. P. O'Boyle, and H. Wickramasinghe, Appl. Phys. Lett. **65**, 1623 (1994).
[12] Y. Inouye and S. Kawata, Opt. Lett. **19**, 159 (1994).
[13] T. Ohta, K. Inoue, M. Uchida, K. Yoshioka, T. Akiyama, S. Furukawa, K. Nagata, and S. Nakamura, Jpn. J. Appl. Phys. **28**, 123 (1989).
[14] For instance, J. W. Goodman, *Introduction to Fourier Optics* (McGraw-Hill, San Francisco, 1986).
[15] H.-J. Butt, C. B. Prater, and P. K. Hansma, J. Vac. Sci. Technol. B **9**, 1193 (1991).
[16] T. Kouyama, K. Kinoshita, Jr., and A. Ikegami, Adv. Biophys. **24**, 123 (1988).

Downloaded 15 Oct 2008 to 130.34.135.158. Redistribution subject to AIP license or copyright; see http://jap.aip.org/jap/copyright.jsp